

UC Davis

Civil & Environmental Engineering

Title

Effect of coefficient of uniformity on cyclic liquefaction resistance of granular materials

Permalink

<https://escholarship.org/uc/item/042876p3>

Authors

Banerjee, Sounik Kumar

Yang, Ming

Taiebat, Mahdi

Publication Date

2023-03-01

DOI

10.1016/j.compgeo.2022.105232

Peer reviewed



Research paper

Effect of coefficient of uniformity on cyclic liquefaction resistance of granular materials

Sounik Kumar Banerjee^a, Ming Yang^{a,b}, Mahdi Taiebat^{a,*}^a Department of Civil Engineering, University of British Columbia, Vancouver, BC, Canada^b Department of Civil and Environmental Engineering, Northwestern University, Evanston, IL, USA

ARTICLE INFO

Keywords:

Cyclic liquefaction
Particle size distribution
Coefficient of uniformity
Relative density
Discrete element method
Granular material

ABSTRACT

Using three-dimensional discrete element method, we analyze the particle size distribution (PSD) effect on the cyclic liquefaction resistance of spherical particle assemblies. For the same mean particle size and log-linear type PSD, the coefficient of uniformity (C_u) is chosen as a descriptor of the PSD. Samples with five levels of C_u are isotropically compressed to the same pressure and two relative densities (D_r) informed by the maximum and minimum achieved void ratios determined for each C_u . The ten samples are subjected to constant volume cyclic simple shearing at different cyclic stress ratios until reaching initial liquefaction, in 56 simulations. The simulations suggest that at each D_r , the evolution pattern of excess pore pressure ratio against the number of loading cycles normalized by the number of cycles to liquefaction is minimally affected by the C_u . For the samples with lower D_r , increasing the C_u in the range 1–3 first increases and then decreases the liquefaction resistance; this trend reverses at the higher D_r . Two critical state parameters based on the void ratio and the coordination number at the pre-shearing state of the samples correlate well with the cyclic liquefaction resistance for the ranges of C_u and D_r considered in this study.

1. Introduction

Cyclic liquefaction in saturated granular soils can lead to a significant reduction of the shear resistance and induce a considerable accumulation of shear strain (Seed and Lee, 1966; Peacock and Seed, 1968), causing catastrophic damage to infrastructure. Many factors affect the liquefaction resistance of granular soils, including but not limited to soil type, density, confining stress, initial static shear, inherent fabric, and drainage condition (e.g., Castro and Poulos, 1977; Vaid et al., 1985; Ishihara, 1993; Chiaro et al., 2012; Wichtmann and Triantafyllidis, 2016; Vargas et al., 2020). Here, the soil type implies the intrinsic factors of the grains, such as particle mineralogy, particle size distribution (PSD), and particle shape. An ideal investigation of the effect of these factors on the cyclic liquefaction resistance of granular materials would require the isolation of their impact – something that is very challenging, if at all possible, in the laboratory testing of soils.

Among these particle characteristics, the effect of PSD on the cyclic liquefaction resistance of some soils has been investigated through laboratory experiments. Vaid et al. (1990) initiated the isolation of particle size distribution, quantified by the coefficient of uniformity C_u , from other factors such as mean particle size D_{50} , PSD curve shape, and mineralogy. Three medium sands of varying gradations, with C_u in the range of 1.5–6, and the same mean particle size and log-linear PSD

curves were formed and cyclically sheared at the same relative densities in the undrained triaxial setting. They reported that at low relative densities, an increase in C_u tends to increase the liquefaction resistance, while the trend is opposite at high relative densities. Kokusho et al. (2004) prepared sand samples with similar minimum particle size D_{min} and PSD curve shapes, but different C_u in the range of 1.5–13, and studied those in undrained cyclic triaxial tests. Despite the large differences in grading, they reported only a small difference in the cyclic liquefaction resistance for the same relative density, as long as the particles are not crushable. For the weak quality and crushable soil particles, they reported that the cyclic liquefaction resistance tends to decrease with increasing C_u . Yilmaz and Mollamahmutoglu (2009) composed various graded sand samples, all at $D_r = 60\%$, by mixing one subgroup of sand with six others at different percentages of weight. The subgroups were related to those retained between different U.S. standard gradation sieves. In samples of any two different graded sands, the one with a smaller mean grain size D_{50} was more susceptible to liquefaction. For samples with the similar D_{50} , those with a smaller void ratio range were more susceptible to liquefaction. Wei et al. (2020) investigated the liquefaction characteristics of sand-fines mixtures by adding crushed silica fines to base sands at a varying percentage by mass. They studied samples with similar void ratios regardless of their

* Corresponding author.

E-mail address: mtaiebat@civil.ubc.ca (M. Taiebat).

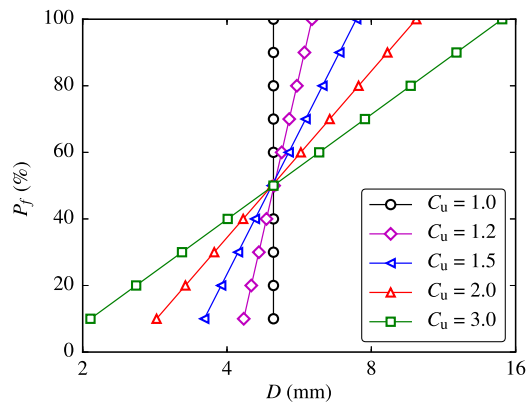


Fig. 1. Particle size distributions used in the study in the form of log-linear variations of percent equal or finer by weight (P_f) versus particle diameter (D), for five C_u values, all with the same D_{50} .

relative densities and observed that liquefaction resistance decreases with increasing the fine content. Cappellaro et al. (2021) studied the liquefaction resistance of the mixtures of sand and non-plastic silt. They reported adding fines reduces the liquefaction resistance at the same relative density, with the reduction being more pronounced for dense specimens. They also showed that the void ratio does not provide a good measure of the effect of density on the liquefaction resistance. They found a good relation between state parameter (Been and Jeffries, 1985) and liquefaction resistance, although they pointed out that this relation is not universal across all the tested soils.

The above examples of experimental laboratory studies provide a primary state of knowledge about the effect of PSD on liquefaction resistance. However, some findings appear contradictory, which may stem from the differences in the soil types, test protocols, the adopted liquefaction criteria, and most notably, the difficulty of the complete isolation of the C_u effect from other contributing factors such as particle shape and surface roughness which are expected to affect the results noticeably. Idealized particles might be advantageous to avoid these concerns. Although similar laboratory experimental studies can be conducted on glass beads or other idealized particles, the discrete element method (DEM) is an excellent numerical approach to investigate the sole effect of PSD on the cyclic liquefaction resistance of granular materials. In addition, DEM makes it convenient to extract and analyze particle-level information and insights, reinforcing the observations from the macroscopic response.

The particle dynamic DEM developed by Cundall and Strack (1979) has been used to explore the effect of PSD on the packing and monotonic shearing properties of granular materials. For instance, increasing C_u will increase the random closest packing fraction of spherical particles but reduce the corresponding coordination number, where more particles have the minimal number of contacts (Taiebat et al., 2017). The force distribution gets increasingly broader with a higher proportion of weak forces when C_u increases. The strong force chains tend to be captured by large particles (Voivret et al., 2009), but large particles do not always carry strong average pressure (Mutabaruka et al., 2019). For samples with continuous PSD curves, Liu et al. (2021) observed a clear correlation between the cumulative distribution of particle sizes by volume and the cumulative distribution of particle sizes by mean effective stress. Voivret et al. (2009) showed that particle size span has negligible effects on the critical state strength, but the proportions of the fabric anisotropy components contributing to the strength may get redistributed for different size spans. Consistently, Yan and Dong (2011) showed C_u has no significant effect on the critical stress ratio, but higher C_u leads to lower positions of the critical-state lines in void ratio vs. mean stress space. This, in turn, is consistent with the observation of Jiang et al. (2018), where they also showed

that increasing C_u decreases critical state coordination number. Phan et al. (2021) showed that static liquefaction resistance increases with increasing fines content up to transition fines content and decreases after that with further increasing fines content.

Over the recent decades, several DEM studies have reported on the cyclic liquefaction of granular materials under constant volume shearing (e.g., Ng and Dobry, 1994; Sitharam, 2003; Wang and Wei, 2016; Barrero et al., 2018; Huang et al., 2019; Yang et al., 2021a, 2022a,b). To the authors' knowledge, isolation of the effect of C_u on the cyclic liquefaction resistance is not yet reported in DEM studies and is a timely topic to be explored. This paper focuses on filling this gap via three-dimensional (3D) DEM. Samples composed of spherical particles with the same mean particle size and five different C_u levels are isotropically compressed to specific pressure and two specific relative densities. The samples are subjected to constant volume cyclic simple shearing at different levels of cyclic stress ratio until initial liquefaction, allowing the identification of their liquefaction susceptibility. Additionally, micromechanical exploration based on particle-level information is exploited to find micro-scale descriptors linked to the observed macroscopic response. It should be noted that the cyclic simple shearing on *isotropically* compressed samples, as considered in this study, mimics the cyclic torsional hollow-cylinder shear tests on isotropically compressed samples in laboratory testing of soils. The simplification of dealing with isotropically compressed samples reduces the complexity associated with the inherent anisotropy that would be present otherwise. This simplified type of test has been used in several experimental (e.g., Tatsuoka et al., 1982; Chiaro et al., 2012; Vargas et al., 2020) and DEM studies (e.g., Kuhn et al., 2014; Wei and Wang, 2017; Zhang and Evans, 2018). The resulting macroscopic response in terms of stress path and stress-strain curve qualitatively looks similar to the conventional simple shear test on uni-axially consolidated (K_0) samples. Whether the test type (such as triaxial or simple shear) or the initial consolidation condition (such as anisotropic consolidation or initial confinement) influence what we conclude in this study deserves further investigation.

2. DEM setup

An open-source DEM code for simulation of particle dynamics LIGGGHTS (Kloss et al., 2012) is used in this paper. Spherical particles are adopted to construct the granular assembly. The spheres interact based on a soft-particle law, allowing slight overlap at the contact point. The contact laws between spheres consist of a Hertzian normal model and a history-dependent tangential model with a Coulomb friction cut-off. The modified elastic-plastic spring dashpot model EPSP2 is used for including the rolling moment for spherical particles (Ai et al., 2011). Details of the contact models can be found in LIGGGHTS documentation. These contact models will introduce parameters including particle Young's modulus E , Poisson's ratio ν , coefficient of restitution ϵ , and coefficient of tangential and rolling friction denoted as μ and μ_r , respectively.

The particle size distributions are adopted in the form of log-linear variations of percent equal or finer by weight (P_f) versus particle diameter (D), for five C_u values (see Fig. 1). These PSD curves share the same D_{50} but differ in the values of coefficient of uniformity $C_u = D_{60}/D_{10}$, where D_x refers to the size that $x\%$ of the particles by volume are not larger than that. For these PSD curves, the C_u is selected as the sole descriptor of PSD. One may question whether D_{50} and PSD curve shape will affect the cyclic liquefaction resistance of the granular system; this aspect is not explored in the current study and deserves future investigation.

Inspired by Voivret et al. (2007), Taiebat et al. (2017) and Mutabaruka et al. (2019), ten distinct classes of particles are constructed to approximate the log-linear PSD curves, corresponding to the discrete markers of each PSD in Fig. 1. Each class consists of particles of the same size, and its number of particles is determined by the class

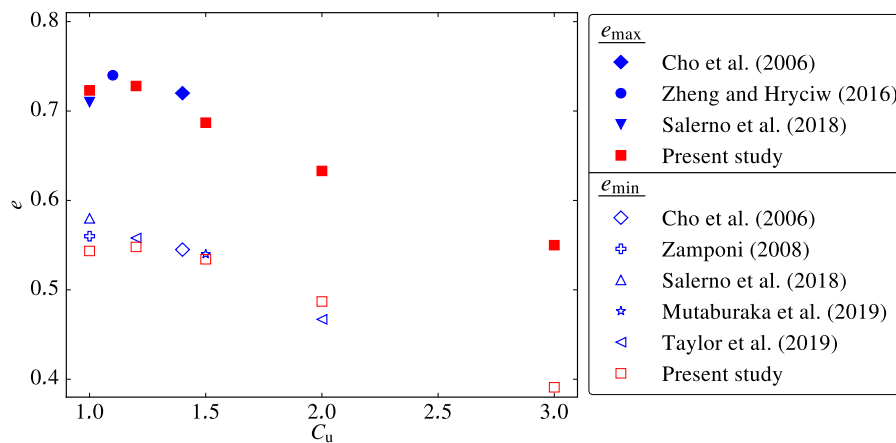


Fig. 2. Maximum and minimum simulated void ratios in this study in comparisons with the reported values in the literature for spherical particles at different levels of C_u .

Table 1
DEM parameters.

Description	Value
Particle density, ρ	2500 kg/m ³
Particle Young's modulus, E	70 GPa
Particle Poisson's ratio, ν	0.25
Tangential friction coefficient, μ	0.5
Rolling friction coefficient, μ_r	0.1
Restitution coefficient, ϵ	0.2

volume and the particle size. The class with the largest particle size will naturally have the smallest number of particles. At least 30 particles are considered in the class of largest particle size to avoid too few particles in this class and to ensure having a statistically fair estimation of the packing state as a whole (Mutabaruka et al., 2019; Banerjee, 2022). At the same time, the larger number of particles in the class of largest particle size would result in a significantly larger number of particles in the class of smallest particle size, and, thus, a much larger number of all particles. On the other hand, incorporating a class with very small particle sizes would lead to the number of particles in the granular system increasing drastically, thereby inducing a significant computational cost. On that basis, here D_{10} is chosen as the minimum particle diameter. As shown in Fig. 1, this study selects five C_u values of 1.0, 1.2, 1.5, 2.0, and 3.0, with the same $D_{50} = 5$ mm. The total number of particles N_p in each C_u are 8 000, 8 000, 9 000, 13 000, and 24 000, respectively. For each PSD, the DEM simulation goes through two stages: (1) sample preparation, where the sample is isotropically compressed to achieve a specific relative density, and (2) shearing process, where the sample is sheared at constant volume and under a certain cyclic stress ratio. The DEM simulation parameters are given in Table 1.

2.1. Sample preparation

To isotropically compress a particle assembly to reach a target mean stress p_0 , a large cubic simulation box is first created in LIGGGHTS. The top and bottom sides of the box are rigid walls, and the four lateral sides are periodic boundaries, denoted as a bi-periodic cell. The gravity is set as zero during the simulation to prevent segregation during compression and shearing. The particles are randomly inserted into the bi-periodic cell, whose dimensions are large enough to have no overlap between the particles. Once the insertion is complete, a servo-control algorithm (e.g., Thornton, 2000) is used to isotropically compress the sample to 10% of the target value p_0 . This initial compression stage is the only stage of the simulation where the tangential friction coefficient μ is tuned to values different from the one listed in Table 1. Then, μ is set to 0.5 as listed in Table 1, and by servo-control isotropic

compression the mean stress is increased to the target value p_0 , that is 100 kPa in this study; this value of μ is also used in the cyclic simple shearing stage. This two-step isotropic compression procedure is adopted from Thornton (2015) as a numerical technique to obtain samples with different densities; the method has also been used more recently by Yang et al. (2021a,b, 2022a,b). In this procedure, setting μ to 0 and 0.5 in the first step of isotropic compression results in samples with extreme void ratios, usually deemed close to the loosest and densest accessible states, respectively (Kuhn et al., 2014). These two extreme void ratios are considered to be the minimum void ratio e_{min} and maximum void ratio e_{max} for the calculation of the relative densities of the samples.

The simulated values of e_{max} and e_{min} obtained in this study are presented in Fig. 2 and compared with those reported by Cho et al. (2006) using glass beads in experiments, and others (Zamponi, 2008; Zheng and Hryciw, 2016; Salerno et al., 2018; Mutabaruka et al., 2019; Taylor et al., 2019) using spherical particles in 3D-DEM simulations. The results are in good agreement with each other. Additionally, one can see how the extreme void ratios change as C_u is increased, demonstrating the importance of considering D_r rather than void ratio e when analyzing the effect of PSD. On that basis, for each PSD, samples with two target relative densities of $D_r = 30\%$ and 50% are constructed to high accuracy by exploiting the value of μ_{prep} iteratively in the range of 0 and 0.5. Therefore, in total, ten samples are prepared covering five levels of C_u and two levels of D_r , all isotropically compressed to $p_0 = 100$ kPa. Using these reduced friction coefficients tends to construct DEM samples with relatively high contact density, compared with samples prepared at similar D_r using typical laboratory sample preparation techniques (Agnolin and Roux, 2007). This effect becomes more pronounced with increasing the sample density. Thus the dense DEM samples following the current sample preparation protocol will manifest considerably higher liquefaction resistance, well above what one would expect from physical tests in the laboratory. Therefore, in this study, we do not consider DEM samples with D_r larger than 50%. As such, the DEM samples with $D_r = 50\%$ in this study are not comparable to the laboratory ones at the same density, given the difference in sample preparation methods; rather, they may be compared with very dense samples prepared in the laboratory. The DEM samples with $D_r = 30\%$ correspond to medium-dense samples prepared in the laboratory. To reduce the high contact density in dense DEM samples, one may consider trying alternative numerical schemes, e.g., assigning a particle coordinate expansion to the dense DEM samples (Agnolin and Roux, 2007), or using a slightly reduced interparticle friction coefficient for sample preparation combined with assigning random velocities to the particles (Kuhn et al., 2014). Table 2 specifies the constructed sample properties, including the tangential friction coefficient for preparing the sample, the void ratio at the end of isotropic compression, and

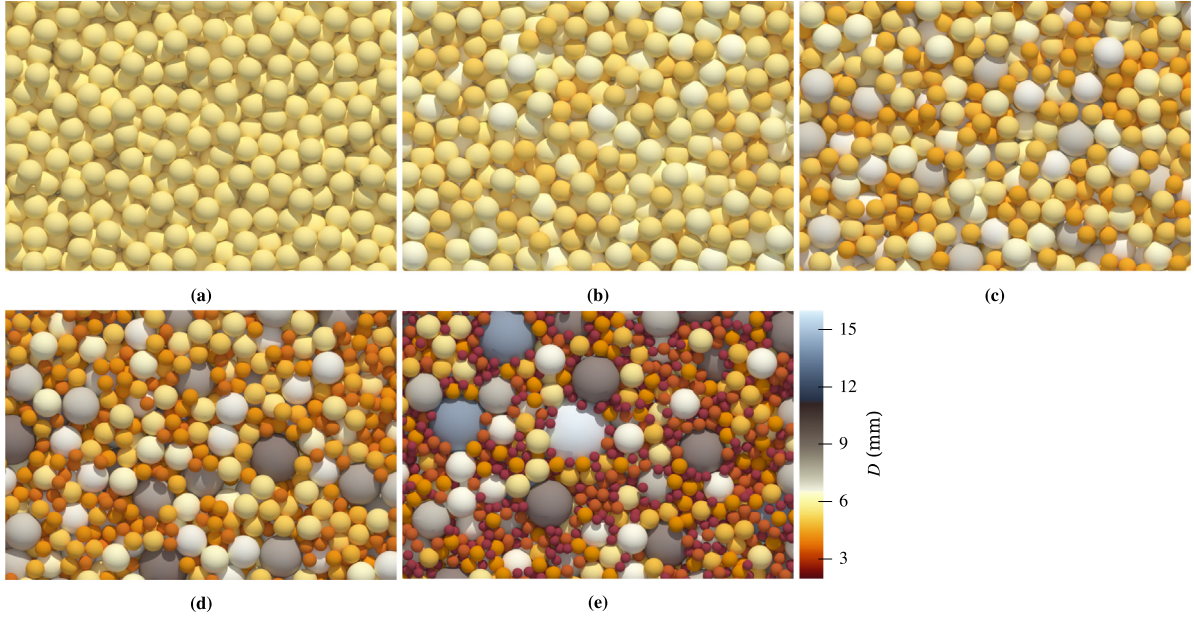


Fig. 3. Snapshot of the samples with coefficient of uniformity corresponding to (a) $C_u = 1.0$, (b) $C_u = 1.2$, (c) $C_u = 1.5$, (d) $C_u = 2.0$, and (e) $C_u = 3.0$, isotropically compressed to $p_0 = 100$ kPa and $D_r = 50\%$.

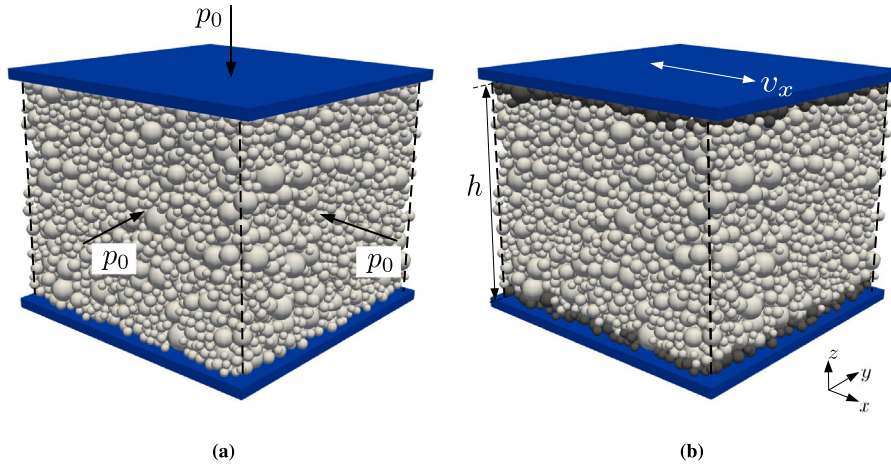


Fig. 4. Schematic representation particle arrangements and boundary condition for one of the tests: (a) at the end of sample preparation under isotropic compression, and (b) during the constant volume cyclic shearing. The gray particles are glued to the top and bottom walls of the simulation cell.

Table 2

Properties of DEM samples isotropically compressed at $p_0 = 100$ kPa.

C_u	μ_{prep}	e_0	$D_r(\%)$	z_0	$a_{c,0}$	$a_{n,0}$	e_{cs}	z_{cs}
1.0	0.292	0.668	30	4.23	0.04	0.05	0.669	3.52
1.0	0.186	0.632	50	4.90	0.02	0.04	0.668	3.48
1.2	0.286	0.670	30	4.58	0.03	0.04	0.623	3.17
1.2	0.181	0.635	50	4.88	0.04	0.05	0.622	3.14
1.5	0.274	0.628	30	4.63	0.03	0.04	0.614	3.24
1.5	0.178	0.602	50	4.85	0.05	0.06	0.613	3.24
2.0	0.271	0.574	30	4.32	0.05	0.05	0.581	2.85
2.0	0.165	0.549	50	4.78	0.06	0.07	0.580	2.84
3.0	0.251	0.473	30	3.92	0.03	0.05	0.468	2.39
3.0	0.139	0.450	50	5.03	0.05	0.07	0.469	2.38

some other descriptors to be explained later in the paper. Fig. 3 shows snapshots of the samples prepared with different C_u and $D_r = 50\%$. Fig. 4(a) displays a sample with $C_u = 2$ isotropically compressed to $D_r = 50\%$ and $p_0 = 100$ kPa.

2.2. Shearing process

In the cyclic shearing stage, the volume of a sample is kept constant by fixing the four lateral periodic boundaries and the bottom wall, and keeping the sample height h constant. Cyclic simple shearing is imposed by moving the top wall horizontally along the x axis at a constant velocity denoted as v_x in forward and backward directions, as shown in Fig. 4. To eliminate slippage between the walls and the sample, a layer of particles is glued to the top and bottom walls, as shown in this figure. The resulting imposed shear strain $\gamma = \gamma_{xz}$ has a sawtooth pattern with the direction of shearing reversed each time the shear stress $\tau = \tau_{xz}$ reaches the target amplitude τ^{amp} , as shown in Fig. 5. The cyclic shearing intensity is quantified by the dimensionless quantity *cyclic stress ratio* (CSR), defined as

$$\text{CSR} = \frac{\tau^{\text{amp}}}{p_0}. \quad (1)$$

The rate of shearing is chosen such that the sample remains in the quasistatic regime based on the inertial number $I = \dot{\gamma}d\sqrt{\rho/p}$, where $\dot{\gamma}$ =

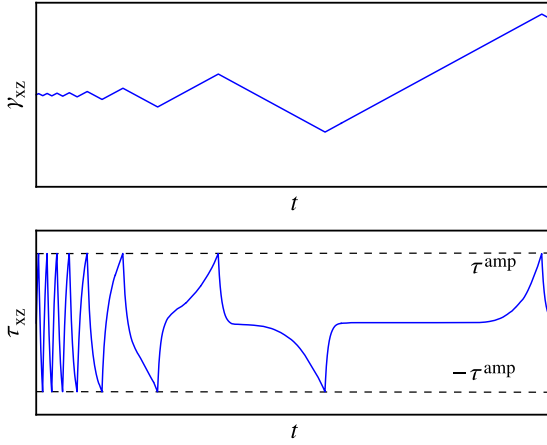


Fig. 5. Loading protocol for the cyclic simple shear with uniform CSR.

$|v_x|/h$ is the shear strain rate, ρ the particle density, d the mean particle size or D_{50} , and v_x is the shear velocity. The shearing is regarded as nearly quasistatic if $I \ll 1$ (MiDi, 2004), and the threshold is typically chosen as 10^{-3} . In this study, we set the top wall $v_x = 1$ mm/s, which results in a maximum shear strain rate $\dot{\gamma} = 0.125$ s $^{-1}$ and the inertial number in the range complying with the quasistatic criterion before the sample liquefies, consistent with Martin et al. (2020). To visualize how momentum is transmitted from top wall particles to the mobile particles of the sheared sample, Fig. 6 presents the shear velocity profile at an instance of shearing just before the peak shear stress for the sample with $C_u = 2$ and $D_r = 30\%$ subjected to CSR = 0.35. In particular, Fig. 6(a) color codes the particle according to their shear velocity, which shows an overall increase of v_x from bottom to top particles. For a better representation of this variation trend, the sample is divided into ten layers along direction z , and the average v_x in each layer against the normalized depth of the sample is presented in Fig. 6(b), indicating a nearly linear relation. When mean stress becomes very small, and the sample liquefies, the well-connected contact network collapses. It was found that further decreasing the shearing rate does not change the macroscopic response noticeably.

The simulated constant volume cyclic simple shear tests in this study are summarized in Table 3. For each sample, at least four simulations are performed. The CSR values for each sample are selected such that the sample reaches initial liquefaction in not much more than about 100 cycles. Each simulation is assigned an ID in the general form of Cu**_Dr**_CSR**. For example, Cu15_Dr50_CSR25 refers to the simulation on a sample with $C_u = 1.5$ and $D_r = 50\%$, subjected to cyclic simple shearing with CSR = 0.25. These numerical experiments allow systematic analysis of how C_u affects the cyclic liquefaction resistance of granular materials. The simulations were carried out on the DesignSafe cyberinfrastructure (Rathje et al., 2017) that is a web-based research and computation platform for the natural hazard engineering community.

3. Macroscopic response

The homogenized stress tensor at the sample scale is used to characterize the overall mechanical response of a particle assembly under constant volume cyclic shearing. Over a given volume V , the stress tensor σ can be expressed as a function of the micro-scale interaction between particles as:

$$\sigma = \frac{1}{V} \sum_{i \in N_c} l^i \otimes f^i, \quad (2)$$

where the branch vector l^i connects the centers of two particles, f^i is the contact force, \otimes refers to the tensor dyadic product, and the

Table 3

Simulated constant volume cyclic simple shear tests on samples with different C_u , D_r , and CSR.

C_u	D_r (%)	CSR
1.0	30	0.10, 0.15, 0.20, 0.25, 0.30
1.0	50	0.30, 0.35, 0.40, 0.45, 0.50, 0.55, 0.60
1.2	30	0.15, 0.20, 0.25, 0.30
1.2	50	0.30, 0.35, 0.40, 0.45, 0.50, 0.55, 0.60
1.5	30	0.15, 0.20, 0.25, 0.30
1.5	50	0.30, 0.35, 0.40, 0.45, 0.50, 0.55, 0.60
2.0	30	0.15, 0.20, 0.25, 0.30
2.0	50	0.30, 0.35, 0.40, 0.45, 0.50, 0.55, 0.60
3.0	30	0.15, 0.20, 0.25, 0.30
3.0	50	0.30, 0.35, 0.40, 0.45, 0.50, 0.55, 0.60

summation includes all the contacts N_c in the selected volume V . In the simple shear test, the shear stress τ and mean effective stress p are given by $\tau = \sigma_{xz}$, and $p = (\sigma_{xx} + \sigma_{yy} + \sigma_{zz})/3$, respectively.

While pore water is not explicitly included in the present DEM model, the deduced excess pore pressure in the equivalent truly undrained system with an incompressible pore fluid can be computed as the variation of the simulated reduction in mean effective stress:

$$\Delta u = p_0 - p, \quad (3)$$

and subsequently, the dimensionless excess pore pressure ratio would be:

$$r_u = \frac{\Delta u}{p_0} = 1 - \frac{p}{p_0}, \quad (4)$$

The shear strain γ is measured as:

$$\gamma = \frac{x_w}{h}, \quad (5)$$

where, x_w refers to the cumulative horizontal displacement of the top wall along x direction:

$$x_w(t) = \int_0^t v_x dt. \quad (6)$$

As observed earlier in Fig. 5, for the adopted loading protocol with constant $\dot{\gamma}$ between the shear reversals at $\pm \tau^{amp}$, the time interval $T/2$ between two successive shear reversals varies in different cycles of shearing. Considering $T(N)$ as the duration of cycle N and t_N its initial time, to present the evolution of a quantity such as r_u , a fractional cycle number N' is used to replace the current running time t by interpolation between two successive cycles:

$$N' = N + \frac{t - t_N}{T(N)}. \quad (7)$$

The value of N' coincides with N at $t = t_N$, and increases by one unit at $t = t_N + T$. To avoid confusion, hereafter, the symbol N is used to represent the fractional cycles as defined by N' .

3.1. Stress and strain response

Fig. 7 presents the typical macroscopic behavior for simulation Cu20_Dr50_CSR35 in terms of stress path and stress-strain curve, as well as the evolution of the deduced excess pore pressure ratio and shear strain development as functions of the number of cycles. The stress path starts from $p = 100$ kPa and $\tau = 0$ kPa, and the stress-strain curves start from the origin. In cyclic shearing, the stress path moves up and down periodically around $\tau = 0$ kPa and between $\pm \tau^{amp}$, and generally moves leftwards, implying an overall decreasing p (or increasing r_u), i.e., an overall contraction tendency of the granular system. At each loading cycle, one can observe local fluctuations of p , where increasing corresponds to dilation tendency and decreasing corresponds to contraction tendency. As cyclic shearing continues, eventually, p momentarily drops to very small values close to 0, or r_u gets close to 1.0, i.e., the sample liquefies and cyclic shear strains accumulate. Inspecting

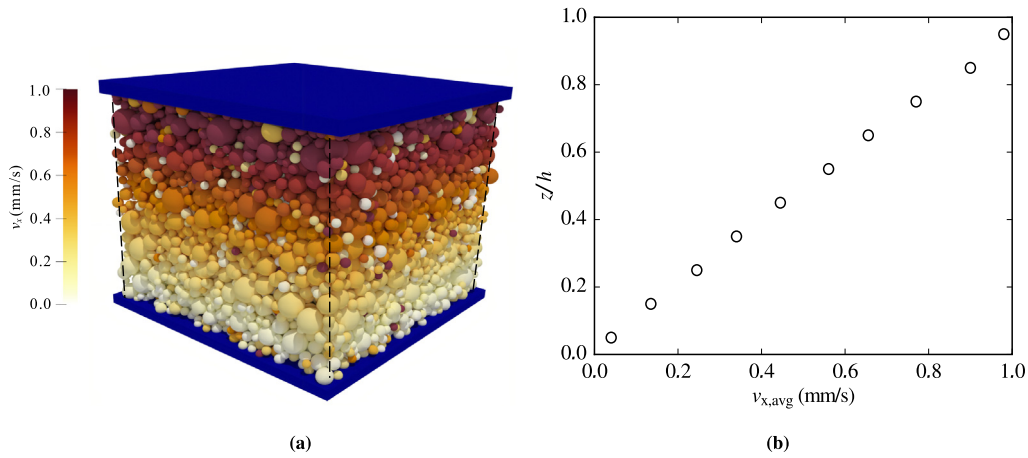


Fig. 6. Shear velocity profile at an instance of shearing just before the peak shear stress for the sample with $C_u = 2$ and $D_r = 30\%$ subjected to $CSR = 0.35$: (a) shear velocity contour plot of all particles, and (b) variation of average shear velocity over the normalized depth of the sample.

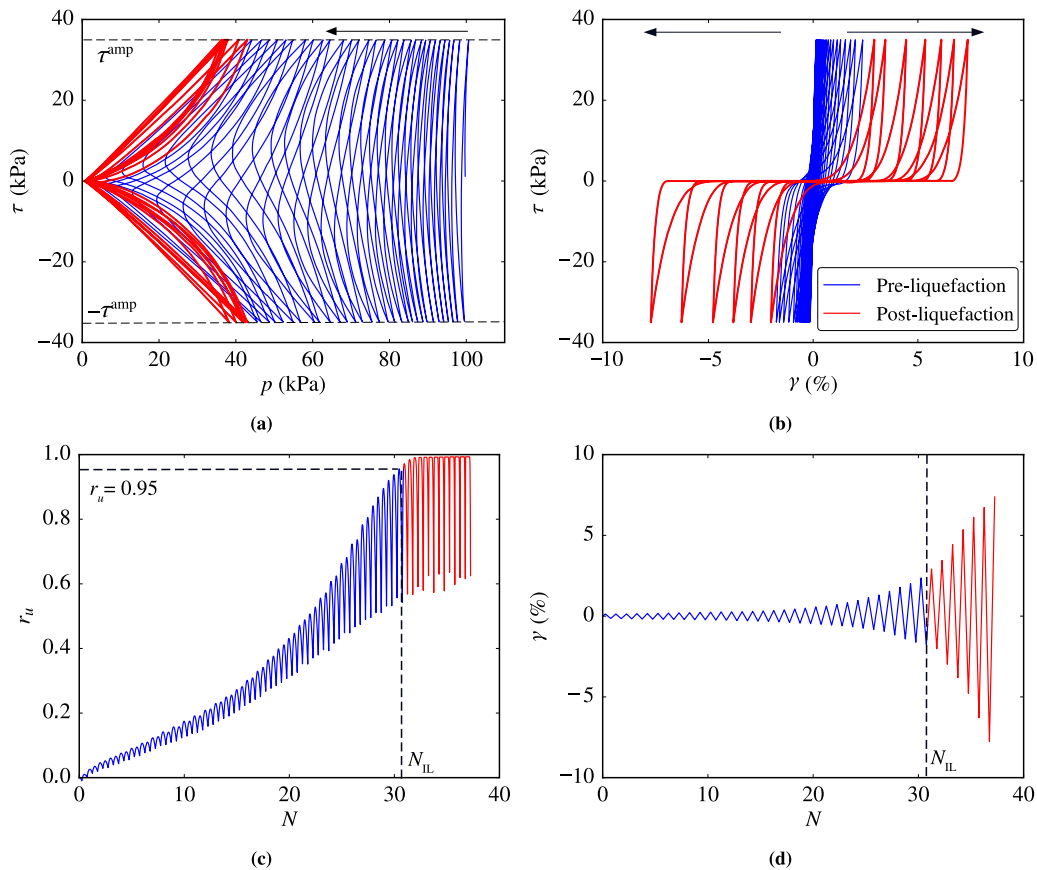


Fig. 7. Macroscopic response of constant volume cyclic simple shear test Cu20_Dr50_CSR35: (a) stress path, (b) stress–strain curve, (c) deduced excess pore pressure ratio evolution, and (d) shear strain development. N_{IL} is the number of cycles to reach initial liquefaction at $r_u > 0.95$, dividing the response to pre- and post-liquefaction.

the stress path of the DEM simulation results reveals that some of them could not closely reach the r_u of 1.0, but when $r_u \geq 0.95$, all simulations present a flow-like response, including accumulation of cyclic shear strains and large deformation. Therefore, the first time r_u exceeds 0.95 is denoted as *initial liquefaction* (IL) in this study, and the corresponding number of cycles to reach this state is labeled as N_{IL} . The shearing periods before and after this state are referred to as pre- and post-liquefaction, respectively. The liquefaction state consists of a loss of stability or load-bearing capacity (both the mean and shear stresses). As described by Yang et al. (2021a), this involves a transition from a solid-like state to a liquid-like state, by analogy with a liquid-saturated

load-bearing granular bed where liquefaction occurs by a transient load transfer from the contact network to the liquid with the development of excess pore pressure. In the pre-liquefaction period, shear strain development is very small, as shown in Figs. 7(b) and 7(d) for $C_u = 2$ at $D_r = 50\%$. In the post-liquefaction period, the stress path gets trapped and oscillates along a butterfly-shaped loop and goes through a nearly transient vanishing of p ; shear strain develops noticeably, especially when r_u gets very close to 1.0, and its amplitude increases with every loading cycle. These observations are consistent with other laboratory experiments and DEM studies.

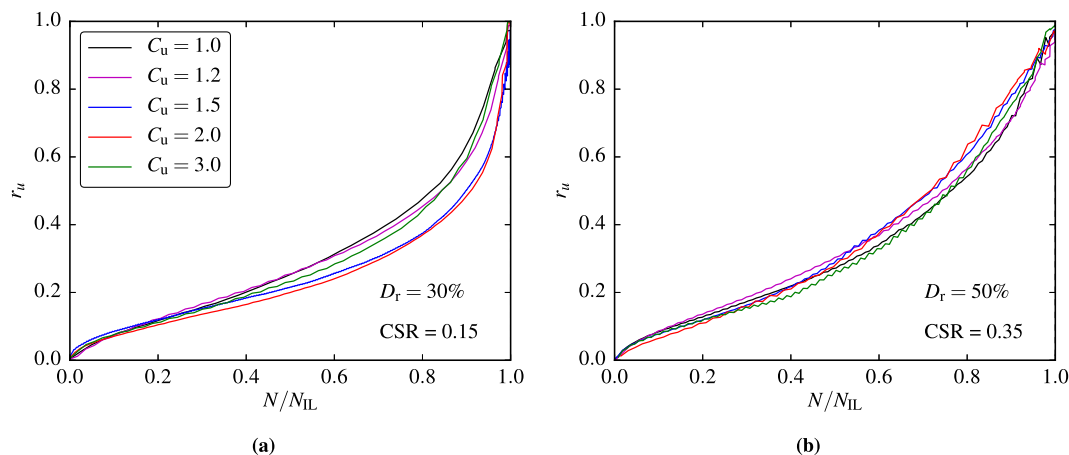


Fig. 8. Effect of C_u on the evolution of deduced excess pore pressure ratio at the beginning and middle of each loading cycle, i.e. near $\tau \approx 0$, for samples with (a) $D_r = 30\%$ & $CSR = 0.15$ and (b) $D_r = 50\%$ & $CSR = 0.35$.

To assess any potential effect of the C_u on the pattern of evolution of deduced excess pore pressure ratio, a total of ten tests are selected covering all studied levels of C_u at either $D_r = 30\%$ and $CSR = 0.15$ or $D_r = 50\%$ and $CSR = 0.35$. Results are presented in Fig. 8 in terms of the evolution of accumulated r_u at the beginning and middle of each loading cycle, i.e., near $\tau \approx 0$, versus the normalized number of cycles to initial liquefaction N/N_{IL} . The selected tests have ten or more pre-liquefaction loading cycles; hence they include sufficient data points between N/N_{IL} of 0 and 1 to have a representative pattern of evolution of r_u . No discernible effect of C_u can be detected on the r_u evolution trends.

3.2. Cyclic liquefaction resistance

Cyclic liquefaction can be triggered by different combinations of uniform CSR, and the number of loading cycles. The liquefaction strength curve, i.e., the plot of CSR versus the number of cycles to the initial liquefaction N_{IL} , often presented in the semi-log scale, is of great practical importance. Fig. 9 presents the liquefaction strength curves of the ten samples. Each data point corresponds to a test on a sample with a given C_u and D_r subjected to a given uniform CSR in a constant volume cyclic simple shear test, as listed previously in Table 3. The discrete data points related to the same sample are fitted by a power-law function (e.g., Idriss and Boulanger, 2008):

$$CSR \propto N_{IL}^{-b} \quad (8)$$

with the exponent b being a fitting parameter. The fitted curves represent the liquefaction strength curves for each sample and are shown by the dashed lines in Fig. 9. The liquefaction strength curves for samples with $D_r = 50\%$ are in the upper right side compared with those for samples with $D_r = 30\%$, implying a higher liquefaction resistance. This is consistent with the expectation that increasing the relative density of granular assemblies will increase their liquefaction resistance. It must be noted that the adopted particle shape, PSD, and sample preparation process have led to higher liquefaction resistance than expected for typical sands at relative densities of 30% and 50%. Inspecting the stress paths and stress-strain loops reveal that all simulations have reached the cyclic mobility mode of deformation.

The effect of C_u on the liquefaction strength curve position is complicated. The trend of this effect varies at different levels of D_r . For samples with $D_r = 30\%$, the liquefaction strength curves are nearly parallel to each other. Increasing the C_u from 1.0 initially results in moving the curve rightwards until $C_u = 1.5$, then leftwards for larger C_u values. This means that at $D_r = 30\%$, the sample with medium polydispersity presents the highest liquefaction resistance. For samples with $D_r = 50\%$, the liquefaction strength curves are intersecting each

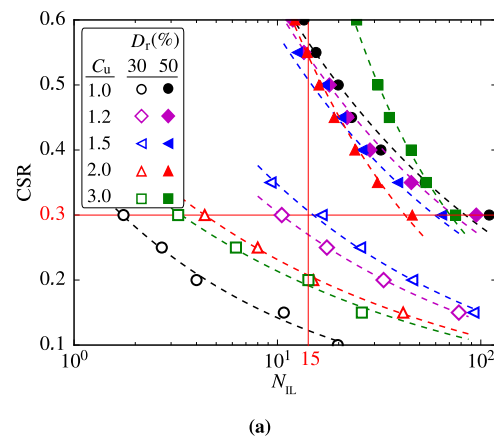


Fig. 9. Cyclic liquefaction strength curves for samples with different C_u and D_r . The dashed lines are power-law fits to the data points. Solid lines at $N_{IL} = 15$ and $CSR = 0.3$ inform the plots of cyclic liquefaction resistance in Fig. 10.

other, meaning that the effect of C_u on N_{IL} depends also on the CSR. One can almost see that increasing C_u from 1.0 initially moves the curve leftwards until $C_u = 2.0$ and further increase in C_u drags the curve rightwards. This means that at $D_r = 50\%$, the sample with medium polydispersity has the lowest liquefaction resistance; contrary to what was observed for $D_r = 30\%$. Additional simulations (not presented here for brevity) were carried out on selected samples to confirm that the randomness of the sample preparation does not affect the conclusions.

There are two common ways to define the cyclic liquefaction resistance of a sample from the cyclic liquefaction curves: (a) the cyclic resistance ratio related to reaching liquefaction at a certain number of cycles, e.g., CRR_{15} that is the CSR required to cause initial liquefaction at 15 loading cycles; and (b) the number of cycles to reach initial liquefaction for a certain CSR, e.g., N_{IL} for $CSR=0.30$. The vertical and horizontal solid lines in Fig. 9 represent these two measures. The CRR_{15} is computed through the interpolation function of Eq. (8). Fig. 10(a) shows the effect of C_u on CRR_{15} for each of the two D_r levels. For samples with $D_r = 30\%$, an increase of C_u from 1.0 initially increased the CRR_{15} until $C_u = 1.5$ and then decreases the CRR_{15} upon further increase of C_u . For samples with $D_r = 50\%$, an increase of C_u from 1.0 initially decreases the CRR_{15} and then increases that beyond $C_u = 2.0$. Similar observations can be made in Fig. 10(b) depicting the relation between N_{IL} for $CSR = 0.30$ and C_u .

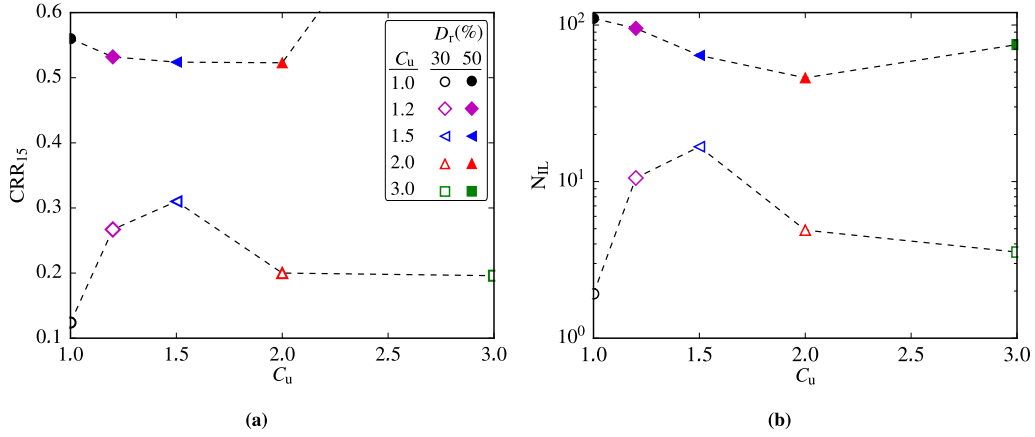


Fig. 10. Effect of C_u on cyclic liquefaction resistance quantified by (a) CRR_{15} and (b) N_{IL} corresponding to $CSR = 0.30$.

4. Linking with the initial state

This section is focused on exploring selected macroscopic quantities and micro-scale descriptors that represent the internal structure of the granular system and assessing the consistency of their trends of variation with the findings of how C_u affects the cyclic liquefaction resistance as presented in Fig. 10. The effects of C_u of CRR_{15} are thought to be attributed mainly to the inherent properties of the samples; therefore, we limit the exploration to the packing properties of the samples at the beginning of the constant volume cyclic shearing stage.

4.1. Initial void ratio, coordination number, and anisotropies

We start by considering the initial void ratio as a macroscopic measure of sample density, and the initial coordination number as a lowest-order scalar descriptor quantifying the contact network. The void ratio is the volume of voids normalized by the volume of solids. The average coordination number refers to the average number of contacts per particle and approximates the level of static redundancy in the granular system, i.e., the difference between the number of constraints and the number of degrees of freedom (Thornton, 2015). At any time during shear, there are particles with zero or only one contact. These particles do not extend the contact network, and as pointed out by Thornton (2000) they do not contribute to the stable state of stress. On this basis, Thornton (2000) defined a mechanical average coordination number as

$$z_m = \frac{2N_c - N_p^1}{N_p - N_p^0 - N_p^1}, \quad (9)$$

where N_c and N_p are the numbers of contacts and particles, respectively, and N_p^0 , N_p^1 are the numbers of particles with zero or only one contact, respectively. One can refer to the fourth and fifth columns of Table 2 to note the initial void ratios and mechanical coordination number of the samples with different C_u values. Apart from the density, and the average number of contacts, contact orientation is an important metric that can influence cyclic liquefaction resistance, as pointed out by Wei and Wang (2017). Two main scalar descriptors of anisotropy are contact anisotropy (a_c) and normal force anisotropy (a_n).

The geometrical anisotropy in a granular system can be described by a second-order fabric anisotropy tensor ϕ_c , which represents the distribution of contact normals \mathbf{n} (Oda, 1982), and defined as

$$\phi_c = \frac{1}{N_c} \sum_{k \in N_c} \mathbf{n}^k \otimes \mathbf{n}^k, \quad (10)$$

with \mathbf{n}^k representing the contact normal, from which the contact anisotropy tensor \mathbf{a}_c can be defined by

$$\mathbf{a}_c = \frac{15}{2} \left(\phi_c - \frac{1}{3} \mathbf{I} \right), \quad (11)$$

where \mathbf{I} is the second-order identity tensor. The deviatoric invariant of the fabric anisotropy tensor \mathbf{a}_c is used to quantify the contact anisotropy a_c as

$$a_c = \sqrt{\frac{3}{2} \mathbf{a}_c : \mathbf{a}_c}. \quad (12)$$

One can refer to Kanatani (1984) and Guo and Zhao (2013) for the details of derivation. With f_n representing the magnitude of normal contact force, the normal force anisotropy can be extracted from normal force tensor that reflects the distribution of normal contact forces, in the form of a force-weighted fabric tensor defined as

$$\phi_n = \frac{1}{N_c} \sum_{k \in N_c} \frac{f_n^k \mathbf{n}^k \otimes \mathbf{n}^k}{1 + \mathbf{a}_c : (\mathbf{n}^k \otimes \mathbf{n}^k)}, \quad (13)$$

from which the force anisotropy tensor \mathbf{a}_n can be defined as

$$\mathbf{a}_n = \frac{15}{2} \left(\frac{\phi_n}{\text{tr} \phi_n} - \frac{1}{3} \mathbf{I} \right), \quad (14)$$

leading to the normal force anisotropy a_n as

$$a_n = \sqrt{\frac{3}{2} \mathbf{a}_n : \mathbf{a}_n}. \quad (15)$$

Given the isotropic nature of sample preparation in the present study, it is anticipated that the pre-shearing samples will exhibit negligible contact and force anisotropies. This is, in fact, evident from the $a_{c,0}$ and $a_{n,0}$ values reported in Table 2. It can be seen that both of these scalar measures of anisotropy have values well below 0.1, indicating that the samples have very little anisotropy and can be considered isotropic. In addition, the range of variation for both $a_{c,0}$ and $a_{n,0}$ is less than 0.04, indicating that the contact and force orientations of these samples with different size distributions are quite similar. Given these observations, it is clear that initial anisotropy indicators are not a key factor in this study; therefore, they are not explored further here.

Figs. 11(a) and 11(b) show the variations of deduced CRR_{15} with e_0 and z_0 , respectively. A sparingly monotonic relation can be observed in Fig. 11(b). Generally, this trend implies that isotropically compressed samples with a higher initial mechanical coordination number exhibit a higher cyclic liquefaction resistance. A similar observation between N_{IL} at the same CSR and z_0 is made by Morimoto et al. (2021) when investigating the effect of pre-shear on the cyclic liquefaction resistance. But a closer inspection of Fig. 11(b) reveals a discrepancy for samples with $C_u = 1.0$ and 2.0 , or samples with $C_u = 1.0$ and 3.0 , at $D_r = 30\%$. The former two samples share a similar z_0 , but their liquefaction resistances are different. In the latter two samples, the one with a higher z_0 presents a lower liquefaction resistance. These observations on the effects of e_0 or z_0 on CRR_{15} call for exploring other macroscopic quantities and microscopic descriptors that may correlate better with the deduced CRR_{15} for the ranges of PSD and D_r in this study.

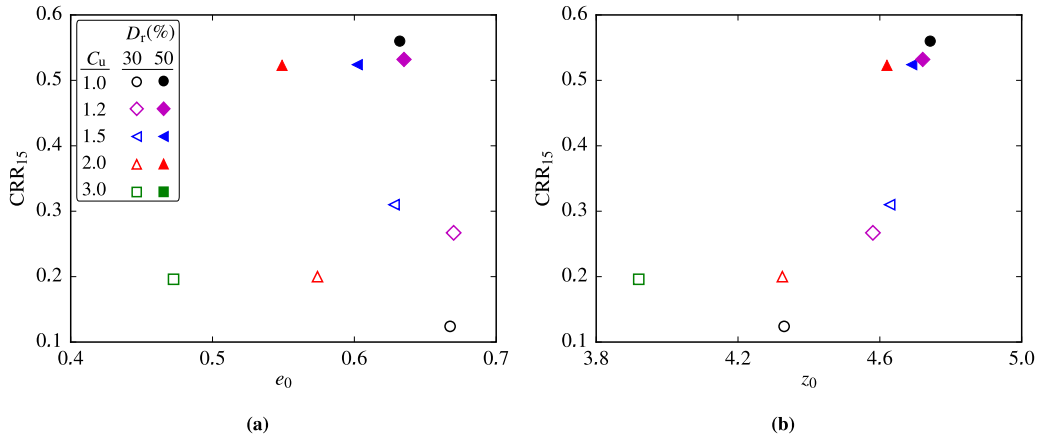


Fig. 11. Variations of (a) initial void ratio e_0 , (b) initial coordination number z_0 for samples with different C_u and D_r .

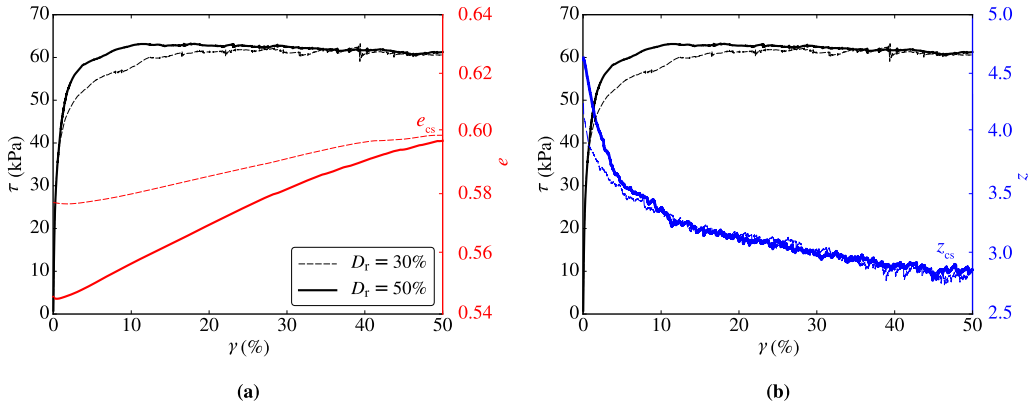


Fig. 12. Evolutions of shear stress τ , void ratio e , and mechanical coordination number z with applied shear strain in drained constant- p monotonic simple shear tests on the samples with $C_u = 2$ and different D_r .

4.2. Initial state parameters

One of the most widely used macro-scale quantities linked with the shear response of sands is the state parameter, which combines the influence of void ratio and stress level with reference to an ultimate (steady) state to describe sand behavior. State parameter ψ as introduced by [Been and Jefferies \(1985\)](#) is the difference between the current void ratio e and the critical state void ratio e_{cs} at the same mean stress p , i.e., $e - e_{cs}$. Let us refer to this void ratio-based macro state parameter as ψ_e , and its initial value at the beginning of the constant volume cyclic shearing stage as $\psi_{e,0}$. It is suggested in some recent studies that the cyclic liquefaction resistance decreases with increasing the initial state parameter $\psi_{e,0}$ despite some scattering in the laboratory experimental data ([Yang and Sze, 2011](#); [Jefferies and Been, 2015](#); [Porcino et al., 2021](#)). A similar trend is also observed in some very recent DEM studies ([Gu et al., 2020](#); [Rahman et al., 2021](#)).

Similar to the definition of macro state parameter ψ_e , one can define a micro state parameter ψ_z as the difference between the current mechanical coordination number z and the critical state mechanical coordination number z_{cs} corresponding to the same p , i.e., $\psi_z = z - z_{cs}$. We refer to the initial value of this mechanical coordination number-based micro state parameter as $\psi_{z,0}$. With reference to some cyclic triaxial DEM tests, [Gu et al. \(2020\)](#) suggested some merits in using such micro state parameter instead of the more conventional macro state parameter for correlation with the cyclic liquefaction resistance, which we will assess for the samples in the present study.

To get the values of $\psi_{e,0}$ and $\psi_{z,0}$ for each sample in this study, we need to determine the e_{cs} and z_{cs} corresponding to the initial confinement p_0 . One approach would be conducting monotonic constant-volume or constant- σ_v shearing simulations until reaching the critical

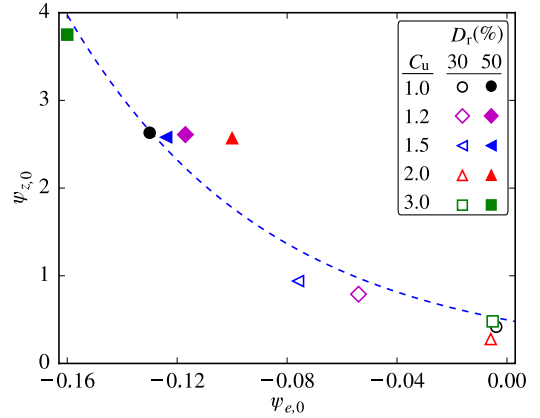


Fig. 13. Relations between $\psi_{e,0}$ and $\psi_{z,0}$ for the samples with different C_u and D_r .

state; in each of these tests, the sample would reach the critical state at a p that is different from p_0 , and therefore one would need several of these tests starting from different initial states to construct the critical state line in the $e - p$ space and subsequently determine the e_{cs} and z_{cs} associated with p_0 . A simpler and more effective approach is followed in this study by conducting a special strain control constant- p shearing protocol for each sample to directly deduce the e_{cs} and z_{cs} corresponding to p_0 . Recall that in analytical terms, the critical state can be expressed as ([Li and Dafalias, 2012](#)):

$$\dot{p} = 0, \dot{s} = 0, \dot{\epsilon}_v = 0 \text{ but } \dot{\epsilon} \neq 0, \quad (16)$$

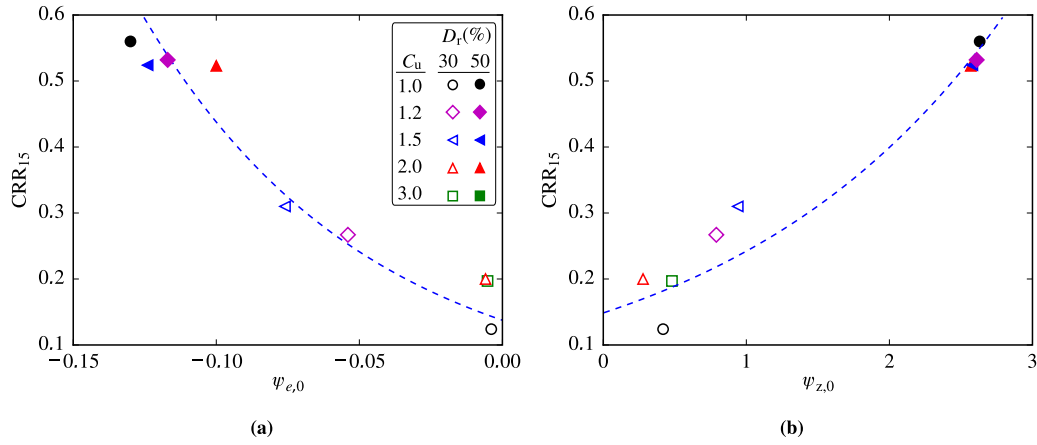


Fig. 14. Variations of (a) initial value of macro state parameter $\psi_{e,0}$ and (b) initial value of micro state parameter $\psi_{z,0}$ with CRR_{15} , for samples with different C_u and D_r .

with \mathbf{s} representing the deviatoric part of the stress tensor, ε_v and \mathbf{e} representing the volumetric strain and the deviatoric part of the strain tensor, respectively, and a superposed dot implying the rate. In this special constant- p strain control shearing protocol, while using bi-periodic boundary conditions for the lateral walls of the sample box, the normal stresses σ_{xx} , σ_{yy} , and σ_{zz} are kept constant using a servo-control algorithm, hence $\dot{p} = 0$, and the sample is sheared under a constant shear velocity applied to the top wall along the x direction, hence a shear strain rate $\dot{\gamma}_{xz}$ within the sample. The corresponding shear strain $\gamma = \gamma_{xz}$ results in variations of shear stress $\tau = \tau_{xz}$ until the sample reaches sufficiently close to the critical state where shear stress τ and void ratio e reach an almost steady state, i.e., $\dot{p} = 0$, $\dot{\mathbf{s}} = \mathbf{0}$ (since $\dot{\tau} = 0$), $\dot{\varepsilon}_v = 0$ (since $\dot{e} = 0$), but $\dot{\mathbf{e}} \neq \mathbf{0}$ due to $\dot{\gamma}_{xz} \neq 0$. The corresponding values of void ratio and coordination number at this state are denoted as e_{cs} and z_{cs} . These values for each sample were listed earlier in Table 2.

Fig. 12 presents the evolutions of shear stress, void ratio, and mechanical coordination number for the samples with $C_u = 2$ at two relative densities, leading to the values of e_{cs} and z_{cs} . As expected, unique values of τ , e_{cs} , and z_{cs} are obtained at sufficiently large levels of shear strain γ for samples with different initial relative densities but the same C_u . The resulting values of $\psi_{e,0}$ and $\psi_{z,0}$ for samples with different C_u and D_r are plotted in Fig. 13, where a unique relation appears to be present between these two quantities, as also seen in Gu et al. (2020).

The relation between CRR_{15} and $\psi_{e,0}$ is displayed in Fig. 14(a), where the data points are fitted by an exponential function. This is consistent with other studies (Yang and Sze, 2011; Gu et al., 2020; Rahman et al., 2021) although they do not consider the effect of C_u . Thus one can see the feasibility of linking cyclic liquefaction resistance with the initial state parameter when considering samples with different C_u . Similarly, Fig. 14(b) shows the relation between CRR_{15} and $\psi_{z,0}$, also fitted by an exponential function. The CRR_{15} reduced non-linearly as $\psi_{e,0}$ increases or the $\psi_{z,0}$ decreases. One can see in Fig. 14(a) that the samples with $\psi_{e,0}$ in the range of -0.10 and -0.13 have almost the same CRR_{15} . Fig. 14(b) shows that these samples in fact share almost the same $\psi_{z,0}$. This is in line with the observation also made by Gu et al. (2020) that the micro state parameter $\psi_{z,0}$ is a more effective state variable that characterizes the initial state effect on cyclic liquefaction resistance than the macro state parameter $\psi_{e,0}$. Inspecting the data points related to $D_r = 30\%$ in Fig. 14(b), it can be observed that the one related to $C_u = 1.0$ is located lower than the fitting line. In particular, this sample has similar initial values of macro and micro state parameters compared with those of $C_u = 2.0$ and 3.0 , but shows lower cyclic liquefaction resistance. We suspect that such low liquefaction resistance may come from the less space-filling in the monodisperse sample compared with the polydisperse ones at low relative density, resulting in a fragile contact network. This, however, cannot be inferred from the initial values of fabric anisotropies $a_{c,0}$ and $a_{n,0}$, coordination number z_0 , and the micro state parameter $\psi_{z,0}$.

5. Conclusions

In this study, we adopted 3D-DEM to investigate the effect of the coefficient of uniformity on the cyclic liquefaction resistance of granular materials, where the coefficient of uniformity C_u is used as the sole descriptor of PSD for assemblies of spherical particles. Isotropic samples with five different values of C_u including 1.0, 1.2, 1.5, 2.0, and 3.0 were prepared under the initial confinement of 100 kPa at relative densities of 30% and 50%. These samples were then subjected to unidirectional cyclic simple shear with different levels of uniform CSR, until reaching the initial liquefaction state. It was observed that at each studied level of relative density, the effect of C_u on the cyclic liquefaction resistance does not have a monotone trend. To more readily assess the effect of C_u , CRR_{15} was adopted as a measure of cyclic liquefaction resistance. At $D_r = 30\%$, an increase of C_u from 1.0 initially increased the CRR_{15} until $C_u = 1.5$ and then decreased the CRR_{15} upon further increase of C_u . For samples with $D_r = 50\%$, the trend became reversed; i.e., an increase of C_u from 1.0 initially decreased the CRR_{15} and then increased that beyond $C_u = 2.0$.

To find the link between the macro-scale observations and the initial state, we extracted initial values of various macroscopic quantities and micro-scale descriptors from the samples prior to cyclic shearing. Initial void ratio and mechanical coordination number did not show a clear trend with the resulting CRR_{15} . Initial contact and normal force anisotropies were too small given the initial isotropic compression of the samples, and, therefore, not reasonable to be explored for their effect on the CRR_{15} . We adopted a protocol for a monotonic simple shear test under constant mean stress to assess the void ratios and mechanical coordination numbers of the samples at the critical state, hence extracting the initial values of the macro and micro state parameters $\psi_{e,0}$ and $\psi_{z,0}$, respectively. These state parameters were observed to present a good monotone relationship with CRR_{15} , irrespective of relative density and coefficient of uniformity. Among these, the state parameter associated with mechanical coordination number appeared to better link with the liquefaction resistance.

CRedit authorship contribution statement

Sounik Kumar Banerjee: Conceptualization, Methodology, Software, Validation, Formal analysis, Investigation, Writing – review & editing, Visualization. **Ming Yang:** Methodology, Validation, Investigation, Writing – review & editing. **Mahdi Taiebat:** Conceptualization, Methodology, Validation, Investigation, Resources, Writing – review & editing, Supervision, Project administration, Funding acquisition.

Declaration of competing interest

The authors declare that they have no known competing financial interests or personal relationships that could have appeared to influence the work reported in this paper.

Data availability

Data will be made available on request.

Acknowledgments

Financial support for this study was provided by the Natural Sciences and Engineering Research Council of Canada (NSERC). We thank Prof. Ellen Rathje for facilitating our access to HPC resources at the Texas Advanced Computing Center. We also thank Dr. Eric Breard for sharing a ray tracing script used in preparing Figs. 3 and 6.

References

- Agnolin, I., Roux, J.N., 2007. Internal states of model isotropic granular packings. I. Assembling process, geometry, and contact networks. *Phys. Rev. E* 76 (6), 061302. <http://dx.doi.org/10.1103/PhysRevE.76.061302>.
- Ai, J., Chen, J.F., Rotter, J.M., Ooi, J.Y., 2011. Assessment of rolling resistance models in discrete element simulations. *Powder Technol.* 206 (3), 269–282. <http://dx.doi.org/10.1016/j.powtec.2010.09.030>.
- Banerjee, S., 2022. Effects of Particle Size Distribution and Particle Shape on Cyclic Liquefaction Response of Granular Materials (Ph.D. thesis). The University of British Columbia, Vancouver, Canada. <http://dx.doi.org/10.14288/1.0413026>.
- Barrero, A.R., Oquendo, W., Taiebat, M., Lizcano, A., 2018. Cyclic shearing response of granular material in the semi-fluidized regime. In: *Geotechnical Earthquake Engineering and Soil Dynamics V: Numerical Modeling and Soil Structure Interaction*. American Society of Civil Engineers, Reston, VA, pp. 100–107. <http://dx.doi.org/10.1061/9780784481479.010>.
- Been, K., Jefferies, M.G., 1985. A state parameter for sands. *Géotechnique* 35 (2), 99–112. <http://dx.doi.org/10.1680/geot.1985.35.2.99>.
- Cappellaro, C., Cubrinovski, M., Bray, J.D., Chiaro, G., Riemer, M.F., Stringer, M.E., 2021. Liquefaction resistance of Christchurch sandy soils from direct simple shear tests. *Soil Dyn. Earthq. Eng.* 141, 106489. <http://dx.doi.org/10.1016/j.soildyn.2020.106489>.
- Castro, G., Poulos, S.J., 1977. Factors affecting liquefaction and cyclic mobility. *J. Geotech. Eng. Div.* 103 (6), 501–516. <http://dx.doi.org/10.1061/AJGEB6.0000433>.
- Chiaro, G., Koseki, J., Sato, T., 2012. Effects of initial static shear on liquefaction and large deformation properties of loose saturated Toyoura sand in undrained cyclic torsional shear tests. *Soils Found.* 52 (3), 498–510. <http://dx.doi.org/10.1016/j.sandf.2012.05.008>.
- Cho, G.C., Dodds, J., Santamarina, J.C., 2006. Particle shape effects on packing density, stiffness, and strength: natural and crushed sands. *J. Geotech. Geoenviron. Eng.* 132 (5), 591–602. [http://dx.doi.org/10.1061/\(asce\)1090-0241\(2006\)132:5\(591\)](http://dx.doi.org/10.1061/(asce)1090-0241(2006)132:5(591)).
- Cundall, P.A., Strack, O.D.L., 1979. A discrete numerical model for granular assemblies. *Géotechnique* 29 (1), 47–65. <http://dx.doi.org/10.1680/geot.1979.29.1.47>.
- Gu, X., Zhang, J., Huang, X., 2020. DEM analysis of monotonic and cyclic behaviors of sand based on critical state soil mechanics framework. *Comput. Geotech.* 128, 103787. <http://dx.doi.org/10.1016/j.compgeo.2020.103787>.
- Guo, N., Zhao, J., 2013. The signature of shear-induced anisotropy in granular media. *Comput. Geotech.* 47, 1–15. <http://dx.doi.org/10.1016/j.compgeo.2012.07.002>.
- Huang, X., Hanley, K.J., Zhang, Z., Kwok, C.y., 2019. Structural degradation of sands during cyclic liquefaction: Insight from DEM simulations. *Comput. Geotech.* 114, 103139. <http://dx.doi.org/10.1016/j.compgeo.2019.103139>.
- Idriss, I.M., Boulanger, R.W., 2008. *Soil Liquefaction During Earthquakes*. Earthquake Engineering Research Institute.
- Ishihara, K., 1993. Liquefaction and flow failure during earthquakes. *Géotechnique* 43 (3), 351–451. <http://dx.doi.org/10.1680/geot.1993.43.3.351>.
- Jefferies, M., Been, K., 2015. *Soil Liquefaction: A Critical State Approach*. CRC Press, <http://dx.doi.org/10.1201/b19114>.
- Jiang, M., Yang, Z., Barreto, D., Xie, Y., 2018. The influence of particle-size distribution on critical state behavior of spherical and non-spherical particle assemblies. *Granul. Matter* 20 (4), 1–15. <http://dx.doi.org/10.1007/s10035-018-0850-x>.
- Kanatani, K.I., 1984. Distribution of directional data and fabric tensors. *Internat. J. Engng. Sci.* 22 (2), 149–164. [http://dx.doi.org/10.1016/0020-7225\(84\)90090-9](http://dx.doi.org/10.1016/0020-7225(84)90090-9).
- Kloss, C., Goniva, C., Hager, A., Amberger, S., Pirker, S., 2012. Models, algorithms and validation for opensource DEM and CFD-DEM. *Prog. Comput. Fluid Dyn.* 12 (2–3), 140–152. <http://dx.doi.org/10.1504/PCFD.2012.047457>.
- Kokusho, T., Hara, T., Hiraoka, R., 2004. Undrained shear strength of granular soils with different particle gradations. *J. Geotech. Geoenviron. Eng.* 130 (6), 621–629. [http://dx.doi.org/10.1061/\(ASCE\)1090-0241\(2004\)130:6\(621\)](http://dx.doi.org/10.1061/(ASCE)1090-0241(2004)130:6(621)).
- Kuhn, M.R., Renken, H.E., Mixsell, A.D., Kramer, S.L., 2014. Investigation of cyclic liquefaction with discrete element simulations. *J. Geotech. Geoenviron. Eng.* 140 (12), 04014075. [http://dx.doi.org/10.1061/\(asce\)gt.1943-5606.0001181](http://dx.doi.org/10.1061/(asce)gt.1943-5606.0001181).
- Li, X.S., Dafalias, Y.F., 2012. Anisotropic critical state theory: role of fabric. *J. Eng. Mech.* 138 (3), 263–275. [http://dx.doi.org/10.1061/\(ASCE\)EM.1943-7889.0000324](http://dx.doi.org/10.1061/(ASCE)EM.1943-7889.0000324).
- Liu, D., O'Sullivan, C., Carraro, J.A.H., 2021. The influence of particle size distribution on the stress distribution in granular materials. *Géotechnique* 1–15. <http://dx.doi.org/10.1680/jgeot.21.00127>.
- Martin, E.L., Thornton, C., Utili, S., 2020. Micromechanical investigation of liquefaction of granular media by cyclic 3D DEM tests. *Géotechnique* 70 (10), 906–915. <http://dx.doi.org/10.1680/jgeot.18.p.267>.
- MiDi, G.D.R., 2004. On dense granular flows. *Eur. Phys. J. E* 14 (4), 341–365. <http://dx.doi.org/10.1140/epje/i2003-10153-0>.
- Morimoto, T., Otsubo, M., Koseki, J., 2021. Microscopic investigation into liquefaction resistance of pre-sheared sand: Effects of particle shape and initial anisotropy. *Soils Found.* 61 (2), 335–351. <http://dx.doi.org/10.1016/j.sandf.2020.12.008>.
- Mutabaruka, P., Taiebat, M., Pellenq, R.J.M., Radjai, F., 2019. Effects of size polydispersity on random close-packed configurations of spherical particles. *Phys. Rev. E* 100 (4), 042906. <http://dx.doi.org/10.1103/physreve.100.042906>.
- Ng, T.T., Dobry, R., 1994. Numerical simulations of monotonic and cyclic loading of granular soil. *J. Geotech. Eng.* 120 (2), 388–403. [http://dx.doi.org/10.1061/\(ASCE\)0733-9410\(1994\)120:2\(388\)](http://dx.doi.org/10.1061/(ASCE)0733-9410(1994)120:2(388)).
- Oda, M., 1982. Fabric tensor for discontinuous geological materials. *Soils Found.* 22 (4), 96–108. http://dx.doi.org/10.3208/sandf1972.22.4_96.
- Peacock, W.H., Seed, H.B., 1968. Sand liquefaction under cyclic loading simple shear conditions. *J. Soil Mech. Found. Div.* 94 (3), 689–708. <http://dx.doi.org/10.1061/JSEFAQ.0001135>.
- Phan, Q.T., Bui, H.H., Nguyen, G.D., Bouazza, A., 2021. Effect of particle rolling resistance on drained and undrained behaviour of silty sand. *Acta Geotech.* 1–26. <http://dx.doi.org/10.1007/s11440-020-01128-y>.
- Porcino, D.D., Triantafyllidis, T., Wichtmann, T., Tomasello, G., 2021. Application of critical state approach to liquefaction resistance of sand-silt mixtures under cyclic simple shear loading. *J. Geotech. Geoenviron. Eng.* 147 (3), 04020177. [http://dx.doi.org/10.1061/\(ASCE\)GT.1943-5606.0002470](http://dx.doi.org/10.1061/(ASCE)GT.1943-5606.0002470).
- Rahman, M.M., Nguyen, H.B.K., Fourie, A.B., Kuhn, M.R., 2021. Critical state soil mechanics for cyclic liquefaction and postliquefaction behavior: DEM study. *J. Geotech. Geoenviron. Eng.* 147 (2), 04020166. [http://dx.doi.org/10.1061/\(asce\)gt.1943-5606.0002453](http://dx.doi.org/10.1061/(asce)gt.1943-5606.0002453).
- Rathje, E.M., Dawson, C., Padgett, J.E., Pinelli, J.P., Stanzione, D., Adair, A., Arduino, P., Brandenburg, S.J., Cockerill, T., Dey, C., et al., 2017. DesignSafe: new cyberinfrastructure for natural hazards engineering. *Nat. Hazards Rev.* 18 (3), 06017001. [http://dx.doi.org/10.1061/\(ASCE\)NH.1527-6996.0000246](http://dx.doi.org/10.1061/(ASCE)NH.1527-6996.0000246).
- Salerno, K.M., Bolinteanu, D.S., Grest, G.S., Lechman, J.B., Plimpton, S.J., Srivastava, I., Silbert, L.E., 2018. Effect of shape and friction on the packing and flow of granular materials. *Phys. Rev. E* 98 (5), 050901. <http://dx.doi.org/10.1103/PhysRevE.98.050901>.
- Seed, H.B., Lee, K.L., 1966. Liquefaction of saturated sands during cyclic loading. *J. Soil Mech. Found. Div.* 92 (6), 105–134. <http://dx.doi.org/10.1061/JSEFAQ.0000913>.
- Sitharam, T.G., 2003. Discrete element modelling of cyclic behaviour of granular materials. *Geotech. Geol. Eng.* 21 (4), 297–329. <http://dx.doi.org/10.1023/B:GEGE.000006036.00597.0b>.
- Taiebat, M., Mutabaruka, P., Pellenq, R., Radjai, F., 2017. Effect of particle size distribution on 3D packings of spherical particles. *EPJ Web Conf.* 140, 02030. <http://dx.doi.org/10.1051/epjconf/201714002030>.
- Tatsuoka, F., Muramatsu, M., Sasaki, T., 1982. Cyclic undrained stress-strain behavior of dense sands by torsional simple shear test. *Soils Found.* 22 (2), 55–70. http://dx.doi.org/10.3208/sandf1972.22.2_55.
- Taylor, H., O'Sullivan, C., Shire, T., Moinet, W., 2019. Influence of the coefficient of uniformity on the size and frequency of constrictions in sand filters. *Géotechnique* 69 (3), 274–282. <http://dx.doi.org/10.1680/jgeot.17.T.051>.
- Thornton, C., 2000. Numerical simulations of deviatoric shear deformation of granular media. *Géotechnique* 50 (1), 43–53. <http://dx.doi.org/10.1680/geot.2000.50.1.43>.
- Thornton, C., 2015. Granular dynamics, contact mechanics and particle system simulations. *DEM Study Part. Technol. Ser.* 24, <http://dx.doi.org/10.1007/978-3-319-18711-2>.
- Vaid, Y.P., Chern, J.C., Tumi, H., 1985. Confinement pressure, grain angularity and liquefaction. *J. Geotech. Eng.* 111 (10), 1229–1235. [http://dx.doi.org/10.1061/\(ASCE\)0733-9410\(1985\)111:10\(1229\)](http://dx.doi.org/10.1061/(ASCE)0733-9410(1985)111:10(1229)).
- Vaid, Y., Fisher, J., Kuerbis, R., Negussey, D., 1990. Particle gradation and liquefaction. *J. Geotech. Eng.* 116 (4), 698–703. [http://dx.doi.org/10.1061/\(ASCE\)0733-9410\(1990\)116:4\(698\)](http://dx.doi.org/10.1061/(ASCE)0733-9410(1990)116:4(698)).
- Vargas, R.R., Ueda, K., Uemura, K., 2020. Influence of the relative density and K_0 effects in the cyclic response of Ottawa F-65 sand-cyclic Torsional Hollow-Cylinder shear tests for LEAP-ASIA-2019. *Soil Dyn. Earthq. Eng.* 133, 106111. <http://dx.doi.org/10.1016/j.soildyn.2020.106111>.
- Voivret, C., Radjai, F., Delenne, J.Y., El Youssoufi, M.S., 2007. Space-filling properties of polydisperse granular media. *Phys. Rev. E* 76 (2), 021301. <http://dx.doi.org/10.1103/PhysRevE.76.021301>.

- Voivret, C., Radjai, F., Delenne, J.Y., El Youssoufi, M.S., 2009. Multiscale force networks in highly polydisperse granular media. *Phys. Rev. Lett.* 102 (17), 178001. <http://dx.doi.org/10.1103/PhysRevLett.102.178001>.
- Wang, G., Wei, J., 2016. Microstructure evolution of granular soils in cyclic mobility and post-liquefaction process. *Granul. Matter* 18 (3), 1–13. <http://dx.doi.org/10.1007/s10035-016-0621-5>.
- Wei, J., Wang, G., 2017. Discrete-element method analysis of initial fabric effects on pre-and post-liquefaction behavior of sands. *Géotech. Lett.* 7 (2), 161–166. <http://dx.doi.org/10.1680/jgele.16.00147>.
- Wei, X., Yang, J., Zhou, Y.G., Chen, Y., 2020. Influence of particle-size disparity on cyclic liquefaction resistance of silty sands. *Géotech. Lett.* 10 (2), 155–161. <http://dx.doi.org/10.1680/jgele.19.00076>.
- Wichtmann, T., Triantafyllidis, T., 2016. An experimental database for the development, calibration and verification of constitutive models for sand with focus to cyclic loading: part I-tests with monotonic loading and stress cycles. *Acta Geotech.* 11 (4), 739–761. <http://dx.doi.org/10.1007/s11440-015-0402-z>.
- Yan, W., Dong, J., 2011. Effect of particle grading on the response of an idealized granular assemblage. *Int. J. Geomech.* 11 (4), 276–285. [http://dx.doi.org/10.1061/\(ASCE\)GM.1943-5622.0000085](http://dx.doi.org/10.1061/(ASCE)GM.1943-5622.0000085).
- Yang, J., Sze, H.Y., 2011. Cyclic behaviour and resistance of saturated sand under non-symmetrical loading conditions. *Géotechnique* 61 (1), 59–73. <http://dx.doi.org/10.1680/geot.9.P.019>.
- Yang, M., Taiebat, M., Mutabaruka, P., Radjai, F., 2021a. Evolution of granular materials under isochoric cyclic simple shearing. *Phys. Rev. E* 103 (3), 032904. <http://dx.doi.org/10.1103/PhysRevE.103.032904>.
- Yang, M., Taiebat, M., Mutabaruka, P., Radjai, F., 2021b. Geometrical network of granular materials under isochoric cyclic shearing. *EPJ Web Conf.* 249, 11004. <http://dx.doi.org/10.1051/epjconf/202124911004>.
- Yang, M., Taiebat, M., Mutabaruka, P., Radjai, F., 2022a. Evolution of granular media under constant-volume multidirectional cyclic shearing. *Acta Geotech.* 17, 779–802. <http://dx.doi.org/10.1007/s11440-021-01239-0>.
- Yang, M., Taiebat, M., Radjai, F., 2022b. Liquefaction of granular materials in constant-volume cyclic shearing: Transition between solid-like and fluid-like states. *Comput. Geotech.* 148, 104800. <http://dx.doi.org/10.1016/j.compgeo.2022.104800>.
- Yilmaz, Y., Mollamahmutoglu, M., 2009. Characterization of liquefaction susceptibility of sands by means of extreme void ratios and/or void ratio range. *J. Geotech. Geoenviron. Eng.* 135 (12), 1986–1990. [http://dx.doi.org/10.1061/\(ASCE\)GT.1943-5606.0000164](http://dx.doi.org/10.1061/(ASCE)GT.1943-5606.0000164).
- Zamponi, F., 2008. Packings close and loose. *Nature* 453 (7195), 606–607. <http://dx.doi.org/10.1038/453606a>.
- Zhang, L., Evans, T.M., 2018. Boundary effects in discrete element method modeling of undrained cyclic triaxial and simple shear element tests. *Granul. Matter* 20 (4), 60. <http://dx.doi.org/10.1007/s10035-018-0832-z>.
- Zheng, J., Hryciw, R.D., 2016. Roundness and sphericity of soil particles in assemblies by computational geometry. *J. Comput. Civ. Eng.* 30 (6), 04016021. [http://dx.doi.org/10.1061/\(ASCE\)CP.1943-5487.0000578](http://dx.doi.org/10.1061/(ASCE)CP.1943-5487.0000578).